Volume 23
Number 4
21 February 2023
Pages 563–804

Lab on a Chip

Devices and applications at the micro- and nanoscale

rsc.li/loc

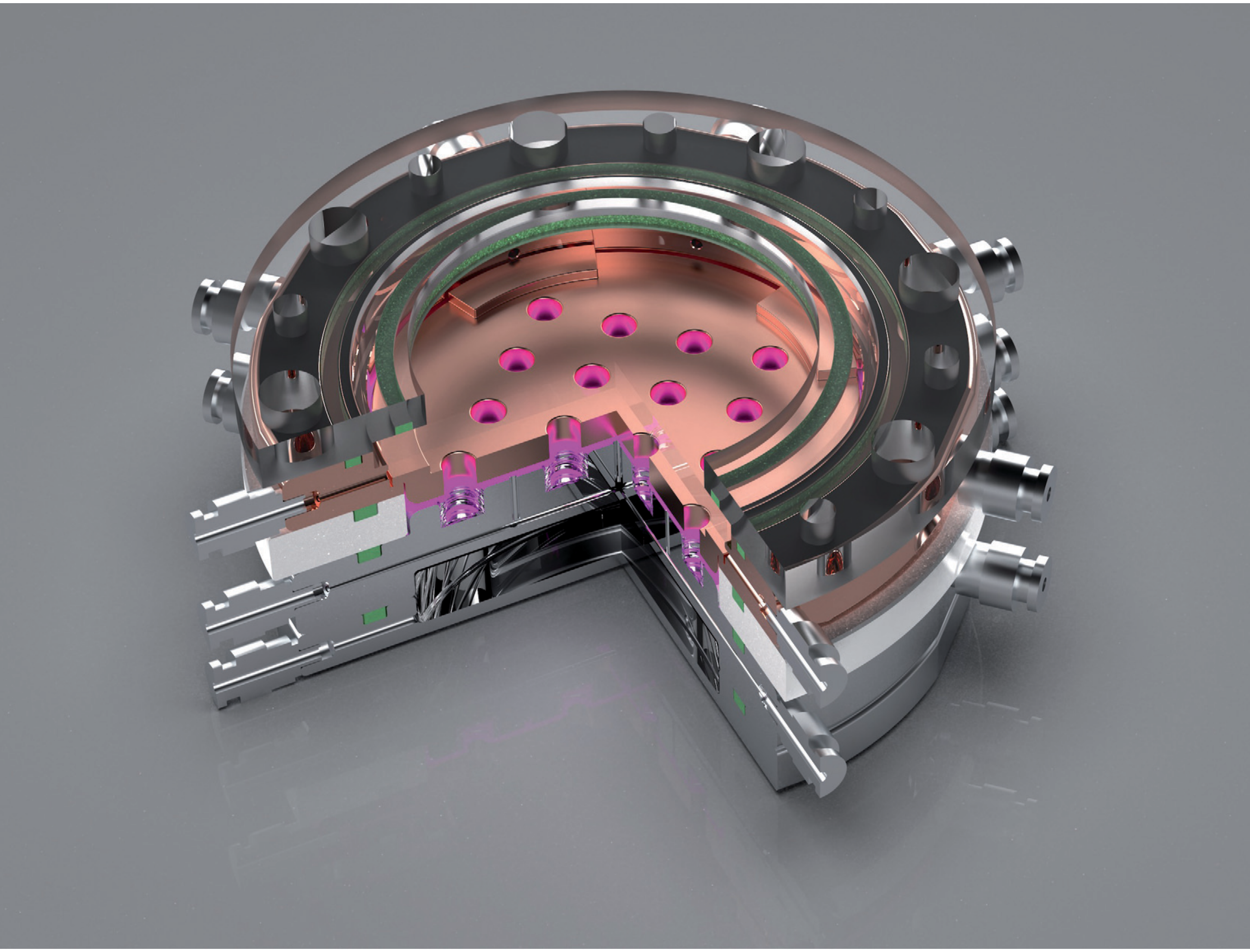

ISSN 1473-0197

ROYAL SOCIETY
OF **CHEMISTRY**

PAPER
Ho Cheung Shum, Hui Deng *et al.*
A composition-tunable cold atmospheric plasma chip for multiplex-treatment of cells

Lab on a Chip

ROYAL SOCIETY OF CHEMISTRY

PAPER

View Article Online
View Journal | View Issue

Check for updates

Cite this: *Lab Chip*, 2023, **23**, 580

A composition-tunable cold atmospheric plasma chip for multiplex-treatment of cells†

Fang Wang,[ab] Chang Li,[b] Ruotong Zhang,[b] Yuan Liu,[b] Haisong Lin,[b]
Lang Nan,[b] Muhammad Ajmal Khan,[a] Yang Xiao,[b]
Ho Cheung Shum*[b] and Hui Deng*[a]

Received 9th October 2022,
Accepted 4th January 2023

DOI: 10.1039/d2lc00951j

rsc.li/loc

Cold atmospheric plasma treatment promises a targeted cancer therapy due to its selectivity and specificity in killing tumor cells. However, the current plasma exposure devices produce diverse and coupled reactive species, impeding the investigation of the underlying plasma–anticancer mechanisms. Also, the limited mono-sample and mono-dosage treatment modality result in tedious and manual experimental tasks. Here, we propose a cold atmospheric plasma chip producing targeted species, delivering multiple dosages, and treating multiple cell lines in a single treatment. Three modules are integrated into the chip. The environment control module and multi-inlet gas-feed module coordinately ignite component-tunable and uniformly distributed plasma. The multi-sample holding module enables multiplex treatment: multi-sample and -dosage treatment with single radiation. By exposing the HepG2 cell line to nitrogen-feed plasmas, we prove the crucial role of nitrogen-based species in inhibiting cell growth and stimulating apoptosis. By loading four-type cell lines on our chip, we can identify the most vulnerable cell line for plasma oncotherapy. Simultaneously, three-level treatment dosages are imposed on the cells with single radiation to optimize the applicable treatment dosage for plasma oncotherapy. Our chip will broaden the design principles of plasma exposure devices, potentially help clarify plasma-induced anticancer mechanisms, and guide the clinical application of plasma-based oncotherapy.

Introduction

Due to the high mortality rate of cancer, many therapeutic methods are developed for cancer treatment.[1–5] Among them, cold atmospheric plasma has emerged as a promising candidate since it can selectively kill cancer cells without damaging healthy cells.[6–8] Plasma exposure can exert various influences on cancer cells, including proliferation reduction, apoptosis induction, mitochondria dysfunction, DNA damage, immune cell death, and gene expression abnormality both *in vitro* and *in vivo*.[9–12] However, the working principles of plasma-induced anticancer remain unclear due to the lack of specifically designed plasma exposure devices, hindering its further clinical application.[13]

Plasma is a type of ionized gas, containing abundant charged ions, radicals, neutral particles, electrical and magnetic fields, and ultraviolet radiation.[14–16] Among them, the highly reactive oxygen species (O, O_2^-, $^1O_2$, OH*, O_3, H_2O_2) and nitrogen species (NO, NO_2^-, NO_3^-, $OONO^-$) are demonstrated as the main contributors to cell death.[17,18] Specific roles of those reactive oxygen and nitrogen species (RONS) are extensively analyzed aiming to enhance the understanding of the plasma anticancer mechanisms. The directly produced short-lived species including $^1O_2$, O^{2-}, OH*, $ONOO^-$ can kill cells by causing lipid peroxidation or damaging antioxidant enzymes, functional molecules, DNA, and RNA.[19–22] The secondly produced $^1O_2$ by long-lived hydrogen peroxide and nitrite capably triggers malignant cells to generate more intracellular RONS, disrupting the antioxidant system and terminally provoking apoptosis pathways.[23–26] In addition, the elevated-expressed aquaporin proteins on the cell membrane could sensitize the cancerous cells to plasma-produced hydrogen peroxide.[27] Recently, physical factors of electromagnetic waves are reported to cause rapid leakage of bulk solutions from the cells, resulting in cytoplasm shrinkage and bubbling on the cell membrane.[28,29] Even though the generation, transportation, and biological effects of the RONS are intensively studied, their roles still cannot be well testified and explained. This is

---

[a] *Department of Mechanical and Energy Engineering, Southern University of Science and Technology, No. 1088, Xueyuan Road, Shenzhen, Guangdong, China. E-mail: dengh@sustech.edu.cn*

[b] *Department of Mechanical Engineering, The University of Hong Kong, Hong Kong, China. E-mail: ashum@hku.hk*

† Electronic supplementary information (ESI) available. See DOI: **https://doi.org/10.1039/d2lc00951j**

because, on one hand, the species are highly coupled in the plasma, on the other hand, most of the cell responses are stimulated by the coordinate work of diverse species.[30] To deeply understand what and how the RONS affect cell behaviors, the targeted species must be isolated and investigated separately.[31]

To date, many devices capable of exciting cold atmospheric plasma have been developed for cancer cell treatment,[32–37] but few of them can controllably modulate plasma composition. The current devices either expose the noble-gas-sustained plasma plumes to the ambient air or directly ignite plasma with air. Such open-to-air design threatens plasma components with air impurities, challenging the precise adjustment of plasma components. Several research groups have recognized this tough issue and are devoted to improving the plasma-exciting modalities to eliminate air influences. Shielding plasma with a noble gas[38,39] could effectively protect plasma from air species contamination, but the high-speed gas stream can potentially dry and mechanically damage the cells.[40] Igniting plasma in a sealed climate chamber is another alternative approach to avoiding the air mixing.[41,42] Without air inflow, deterministic plasma components are attained by feeding proper source gases. Also, in this manner, the high-speed shielding gas is avoided.

Plasma jet is the most prevalently applied modality due to its convenient and flexible operation. However, the small dimension of the plasma bullet determines the inefficient mono-sample treatment capacity, leading to tedious and manual experimental tasks. Another deficiency of plasma jet is that the unevenly distributed RONS in the plasma jet cocktail can result in nonuniform plasma treatment to the cells. Well-documented reports have proved that cell responses can be significantly affected by the treatment dosages.[43] The nonuniform plasma treatment on cells undoubtedly damages the accuracy of the experiment results, especially for the mechanism exploration research. By contrast, surface plasma, ignited between parallel electrodes with a large discharge area, can produce uniformly distributed plasma plumps. The evenly distributed plasma and the relatively large discharge area of surface plasma enable uniform and multi-sample treatment with one-time radiation simultaneously.

As indicated by the preceding discussions, precise control of plasma components, high-efficiency sample treatment capacity, and uniform treatment of cells are the deterministic requirements of plasma igniting devices. In this work, by igniting a surface discharge in the climate chamber, we develop a composition-tunable cold atmospheric plasma chip for multiplex treatment on cells. The proposed chip mainly consists of an environment control module, a multi-inlet gas-feed module, and a multi-sample holding module. The environment control module constrains the plasma in a sealed chamber, eliminating the admixing of air impurities. Through adjusting feed gas mixtures, oxygen-based and nitrogen-based species can be separated. The multi-inlet gas-fee module scatters the feed gas in the sealed chamber uniformly, initiating homogeneous and stabilized plasmas. The evenly dispersed plasma facilitates the uniform treatment of cells. The multi-sample holding module enables multiplex treatment: multi-sample and multi-dosage treatment within one-time radiation. Such a design substantially improves the sample processing capacity of the chip. With this chip, we discover that the nitrogen-feed plasmas worsen cell health more remarkably than oxygen-feed plasma, denoting the nonnegligible role of the nitrogen-based species in plasma oncotherapy. As a research tool, our device potentially enables the subsequent analysis of cell epigenetic and genetic changes after treatment to unveil more profound mechanisms. Benefiting from the multiplex treatment capability, we can efficiently select the most vulnerable cells from the loaded four-type cell lines. The applicable dosage can also be efficiently optimized from the imposed three-level dosages in single radiation. Those explored target cancer types and treatment conditions can guide the clinical application of plasma oncotherapy. Moreover, the rapid development of cancer immune therapy could take advantage of our device as a promising platform to produce vaccines, realizing clinical application.[35] Our chip will inspire the development of effective and efficient plasma exposure devices.

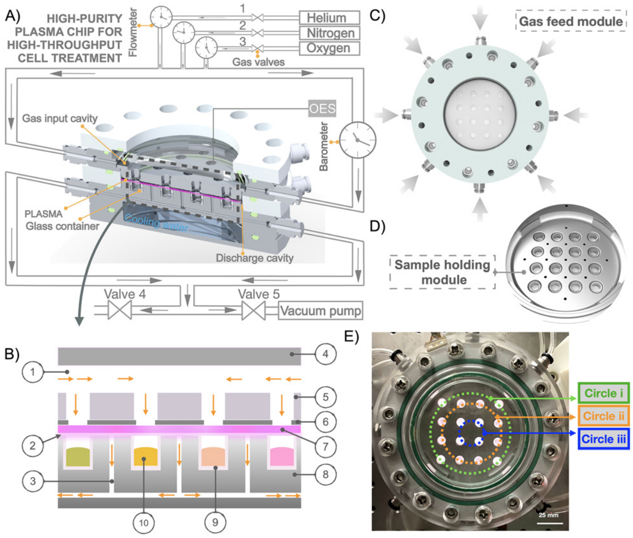

Fig. 1 Schematic illustrating the design and structure of the plasma igniting chip. (A) The 3D-sectional view of the high-purity plasma exciting chip. (B) The 2D-enlarged sectional view of the chip (1: gas input cavity, 2: discharge cavity, 3: gas channel, 4: observation window, 5: power electrode, 6: quartz dielectric barrier, 7: plasma, 8: ground electrode, 9: glass receptacle, 10: liquid sample). (C) The multi-inlet gas-feed module (the top view of the chip). (D) The multi-sample holding module. (E) Graph of the cold atmosphere plasma chip in working condition to demonstrate the central-symmetrically arranged 16 sample-holding wells situated on three concentric circles (circle i with a radius of 30 mm, circle ii with a radius of 22 mm, circle iii with a radius of 10 mm).

Results and discussion

Design principles of the plasma igniting chip

The design principles and work mechanisms of the proposed chip are shown in Fig. 1. To isolate the ignited plasma from the surrounding atmosphere environment, constituent parts of the chip are screwed together with seal rings. The sealed interior cavity of the chip together with a vacuum pump constitute the environment control module. The environment control module can controllably modulate plasma components by adjusting source gases and reducing air species contamination. Before plasma ignition, the internal remaining air was first removed. Then plasma feed gases were injected into the chip with selective switching on valves 1, 2, and 3. Valves 4, 5, and the barometer coordinated to block air from backfilling into the chip during the process of gas replacement. This process can be repeated several times to further diminish the residual air for pure plasma (purple marked line in Fig. 1A and B:7) generation in the discharge cavity (slit between the electrodes Fig. 1A and B:2). In this way, four types of plasmas with controllable components were obtained by feeding plasma with different gases with optimized igniting parameters applied (Table 1). For comparative studies, air plasma without the air replacement process was also excited in our work (Table 2).

Plasma uniformity is guaranteed by the multi-inlet gas-feed module (Fig. 1C), implementing uniform treatment on the cells. This module consists of the gas input cavity (Fig. 1A and B:1, space between the observation window and power electrode) and the central-symmetrically arranged 8 gas inlets. Flowing out of the 8 gas inlets, the feed gas firstly arrives at the input cavity, while the suddenly extended space significantly reduces gas flow velocity (ESI† Appendix, Fig. S1). Through the airholes both on the power electrode (Fig. 1B:5) and the dielectric barrier sheet (Fig. 1B:6), the feed gas could diffuse gently from the gas input cavity to the discharge cavity. Such structure design, on the one hand, improves the equilibrium of the produced plasma for uniform treatment of cells; on the other hand, it alleviates surface agitation caused by the high-speed gas flow.

The multi-sample holding module includes glass receptacles and a sample-holding array sheet (Fig. 1D and ESI† Appendix, Fig. S2), ensuring multiplex treatment. The receptacles can accommodate 100 ml liquid samples and protect the samples from direct contact with the metal surface. The sample holding array sheet allows 16 samples to be processed simultaneously, enhancing radiation efficiency significantly. The 16 wells for sample loading can be seen as situated on three concentric circles, and wells from the same one concentric circle witness identical plasma treatment dosages (Fig. 1E). This is because the feed gas distribution inside of the chip largely depends on gas inlet numbers and display patterns. The 8 central symmetrically assembled gas inlets result in a radius-dependent gas uniformity. Therefore, the wells belonging to different concentric circles will own their unique plasma intensity and the subsequent plasma treatment dosages. In this consideration, we apply the central–symmetrical pattern in the sample-holding array design to hold the receptacles (ESI† Appendix, Fig. S3). In this manner, the limited space is fully utilized to fabricate more wells and multiple plasma treatment dosages are achieved within single radiation. Notably, the pattern of the sample-holding wells displayed here is merely an example to show an appropriate structure design can help manipulate plasma distribution to produce multiple treatment dosages. More advanced patterns can be optimized to suit the ongoing research. Compared with the traditional plasma strength modulation method by adjusting input power, feeding gas species or flow velocity, and the discharge distances, the method of utilizing flow fields to control plasma intensity will make the treatment dosage modulation more efficient and flexible. A water-cooling system is integrated at the bottom of the ground electrode to reduce heat accumulation, as illustrated in Fig. 1A. The cycled flowing ice-cold water keeps carrying away the cumulative heat on the ground electrode, protecting the cells from possibly otherwise damagingly high temperatures. In combination with the design principles mentioned above, an integrated chip that can generate high-purity plasma and achieve multiplex treatment is developed, as shown in ESI† Appendix, Fig. S4.

Tuning plasma components by varying feed gas mixture

To demonstrate the plasma component can be controllably modulated, the excited species were identified and characterized by a spectrometer. As expected, air plasma exhibits the richest plasma chemistry, including nitric oxide (NO, 200–280 nm), hydroxyl radical (OH, 308 nm), molecular nitrogen (N_2, 296 nm, 310–428 nm), helium metastable (He, 706 nm), atomic oxygen (O, 777 nm, and 844 nm) and atomic hydrogen (H, 656 nm) (Fig. 2A). When the chip is evacuated and refilled with pure helium gas, nitrogen-related species disappear, leaving helium as the main signal (Fig. 2B). The disappeared nitrogen-related species are caused by excluding nitrogen gas in the feed gas, while water dissociation produces the remaining oxygen-related species:[44] hydroxyl radicals, atomic oxygen, and atomic hydrogen. With 0.1% oxygen gas admixed into the helium gas, excitation of hydroxyl radical, hydrogen, and helium is suppressed, while

Table 1 Plasma igniting parameters

Discharge area	Input power	Power density	Distance between electrodes	Dielectric barrier
40.17 cm^2	70 W	1.99 W cm^{-2}	2 mm	0.5 mm/quartz

Table 2 Source gas constituent of the ignited plasmas

Plasma definition	Feeding gas	Source gas constituent
Air plasma	Helium (4 L min^{-1}) + residual air	Unknown content of oxygen and nitrogen
Helium plasma	Helium (4 L min^{-1})	No oxygen and nitrogen
Nitrogen plasma	Helium (4 L min^{-1}) + nitrogen (7.2 mL min^{-1})	0.18% (w/w) nitrogen
Oxygen plasma	Helium (4 L min^{-1}) + oxygen (4 mL min^{-1})	0.1% (w/w) oxygen
Oxygen–nitrogen plasma	Helium (4 L min^{-1}) + oxygen (4 mL min^{-1}) + nitrogen (7.2 mL min^{-1})	0.18% (w/w) nitrogen + 0.1% (w/w) oxygen

atomic oxygen excitation increases remarkably (Fig. 2C). The electronegative oxygen captures large amounts of electrons, reducing the available electrons for water dissociation[45] and accordingly, water-derived species. When oxygen is replaced with 0.18% nitrogen gas, molecular nitrogen and hydroxyl radical dominate the spectra (Fig. 2D). In addition, the excitation of nitric oxide is also probed in the nitrogen plasma. Water dissociation generates hydroxy radicals, and these water-derived species contribute to the production of nitric oxide.[46] When a mixture of helium with 0.1% oxygen, and 0.18% nitrogen is fed to the plasma, bands of nitrogen-related species remain the dominant signal lines (Fig. 2E). Compared with nitrogen plasma, the introduction of oxygen gas increases atomic oxygen but suppresses the excitation of hydroxyl radical and nitric oxide. This suggests eliminating air influence is effective in purifying plasma chemistry and producing required species. Helium plasma inclines to produce water-derived hydroxyl radical and atomic oxygen, while oxygen plasma generates strong atomic oxygen species. Nitrogen-related species can be produced by nitrogen plasma. Upon radiation, cells are normally protected by either culture media or some specific buffer solution from dehydration. Therefore, we also measure the signals when plasma is excited with media in the receptacles to assess the influence of the aqueous solution on the plasma components. We find the main species and their relative intensity in the plasma ignited with and without media remain the same when identical feed gases are provided (Fig. 2F–J). The preceding results confirm that our chip can controllably tune plasma chemistry and expose cells to targeted reactive species for studying their biological roles.

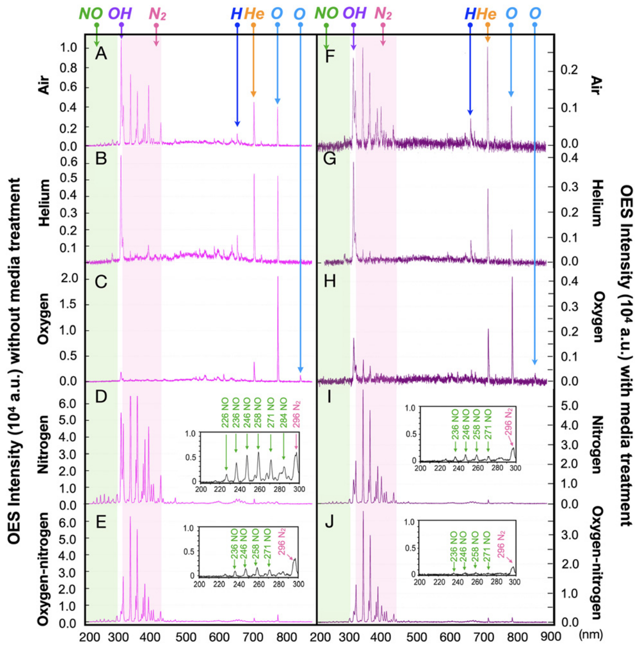

Fig. 2 Graph of the tunable plasma components identified by the OES. (A) Air plasma without media in the receptacles. (B) Helium plasma without media. (C) Oxygen plasma without media. (D) Nitrogen plasma without media. (E) Oxygen–nitrogen plasma without media. (F) Air plasma with media in the receptacles. (G) Helium plasma with media. (H) Oxygen plasma with media. (I) Nitrogen plasma with media. (J) Oxygen-plasma with media. (NO: nitrogen oxide (200–280 nm), OH: hydroxyl (308 nm), N_2: nitrogen (296 nm, 310–450 nm), He: helium (706 nm), O: atomic oxygen (777 nm, 844 nm), H: atomic hydrogen (656 nm)).

Evaluation of plasma stability and uniformity: foundation for multiplex treatment

The proposed multiplex radiation and equivalent dosage delivery largely depend on good stability and uniformity of the plasma. Electrical voltage–current waveform patterns, intensity evolution of excited species, and temperature increases were characterized to demonstrate the stability of the excited plasma. Firstly, monitored by an oscilloscope, we find the voltage and current waveforms transform sinusoidally and periodically, and their amplitudes stabilize at the same value respectively across all probing periods (Fig. 3A and ESI† Appendix, Fig. S5). Then, identified by a spectrometer, we calculated the intensity change of the main excited species to further assess plasma stability. Compared with the intensity measured 0.5 min before, the percentage change of excited helium (706 nm) in helium plasma, molecule nitrogen (337 nm) in nitrogen plasma, atomic oxygen (777 nm) in oxygen plasma, and molecular nitrogen (337 nm) in oxygen–nitrogen plasma fluctuate in the range of 0% to 1.25% (Fig. 3B). As for other observed species in the five types of plasma, their intensity all approaches a constant value, especially within the last 4 minutes of treatment (ESI† Appendix, Fig. S6). At last, we measured the temperature increase of the sample-holding sheet with an infrared thermometer to estimate the heat accumulation. The temperature rises less than 3 °C after the plasma treatment for 5 min, which is completely safe for cell metabolism (Fig. 3C and ESI† Appendix, Fig. S7).[47] So far, the obtained

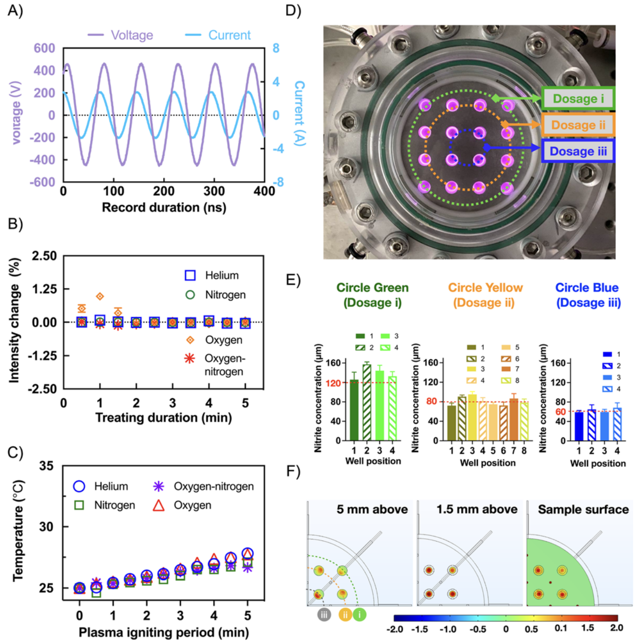

Fig. 3 Plasma stability and uniformity evaluation for multiplex treatment. (A) The waveform of voltage and current of the helium plasma with media in the receptacles. (B) Signal intensity changes of the main excited species in the plasmas during the 5 min treatment duration (excited helium (706 nm) in helium plasma, molecule nitrogen (337 nm) in nitrogen plasma, atomic oxygen (777 nm) in oxygen plasma, and molecular nitrogen (337 nm) in oxygen–nitrogen plasma) (*n* = 3). (C) The temperature change of sample-holding sheet after plasma treatment with media in the receptacles for 5 min. (D) Photograph of the chip in the working station (nitrogen plasma excited) with all wells marked by the dosage circles (green circle for dosage i, yellow circle for dosage ii, blue circle for dosage iii). (E) Nitrite concentration in 100 μL deionized water of the 16 wells after nitrogen plasma treatment for 3 min. Data was obtained from 3 dependent experiments and presented as mean ± SD. (F) Simulation results of the gas flow velocity on the sample surface plane and the planes of 1.5 mm and 5 mm above the sample surface.

results indicate good stability of the ignited plasma, which is an important basis of multiplex treatment.

Benefiting from the arrangement of equidistant sample-holding wells and gas inlets from the centre, the wells belonging to the three concentric circles will be exposed to three different plasma treatment dosages. Here, the three concentric circles are redefined as dosage i (green circle), dosage ii (yellow circle), and dosage iii (blue circle) respectively (Fig. 3D). Plasma uniformity was quantified by measuring the concentration of produced nitrite in 100 μL of deionized water after nitrogen plasma treatment for 3 min. Consistently with the expectation that the same-colored samples produce similar level of nitrite. Green-marked samples generate the most nitrite (around 120 μM), followed by yellow-marked (around 80 μM) and grey-marked (around 60 μM) samples in sequence (Fig. 3E). The result that samples belonging to different circles produce different concentrations of nitrite matches well with the defined radium-dependent uniformity of the plasma. COMSOL simulation further demonstrates that this radium-dependent uniformity is caused by the various gas flow speeds above the sample-holding wells. Wells located in the largest concentric circle (dosage i circle) have the highest flow speed, followed by those located in the medium (dosage ii circle) and the smallest circle (dosage iii circle) in sequence (Fig. 3F). Combined with the produced nitrite, a lower gas flow rate tends to generate more nitrite at the chosen parameters for this device. Clearly, the above demonstrated radium-dependent uniformity enables the multiplex treatment: multi-sample treatment for samples loaded on the same circle, and multi-dosage treatment for samples loaded on different circles. The more vulnerable cell lines can be selected for plasma oncotherapy when different cell lines are loaded on the same circle. Proper treatment dosages for plasma oncotherapy can be explored for the target cancer cell type when loading the same cell line on different circles.

Demonstration of tuning plasma components for cell-death driver species exploration

The influences of different plasmas on HepG2 cells are quantified to demonstrate the significance of modulating plasma components in understanding the roles of the species. Since nitrite and hydrogen peroxide are typical long-living species capable of interacting with cells,[48,49] we first measured their generation after plasma treatment. The samples were loaded, treated, and characterized following the procedures shown in Fig. 4A. Both the generation of nitrite and hydrogen peroxide highly depend on treatment duration: a longer treating period results in higher species concentration. After 5 min treatment, nitrogen and oxygen–nitrogen plasma produce much more nitrite (171.42 mm and 148.61 mM respectively) than helium and oxygen plasma (26.01 mM and 21.32 mM respectively) (Fig. 4B). The same treatment duration of air plasma results in a concentration of 46.32 mM, nearly two times higher than the oxygen and helium plasma, indicating the huge influence of air species on plasma purity. The nitrogen source gas facilitates nitrogen and oxygen–nitrogen plasma to produce nitrogen oxide, resulting in large quantity production of nitrite. While the small volume nitrite generated by the helium and oxygen plasma is caused by insufficient air evacuation. By contrast, only a limited difference in hydrogen peroxide generation (less than 20 mM) is presented among five-type plasmas after treatment for the same duration (Fig. 4C). Since water dissociation contributes to hydrogen peroxide generation significantly,[44] the treated buffer solution with identical volume could be responsible for the equivalent hydrogen peroxide generation of different plasmas.

With our understanding of the species-generating preferences of the purified plasmas, responses of the model cell line were analysed to investigate cell susceptibility towards the diversified plasma components. The afterward-mentioned percentages for cell proliferations rates were all normalized to the control group. We find that compared with

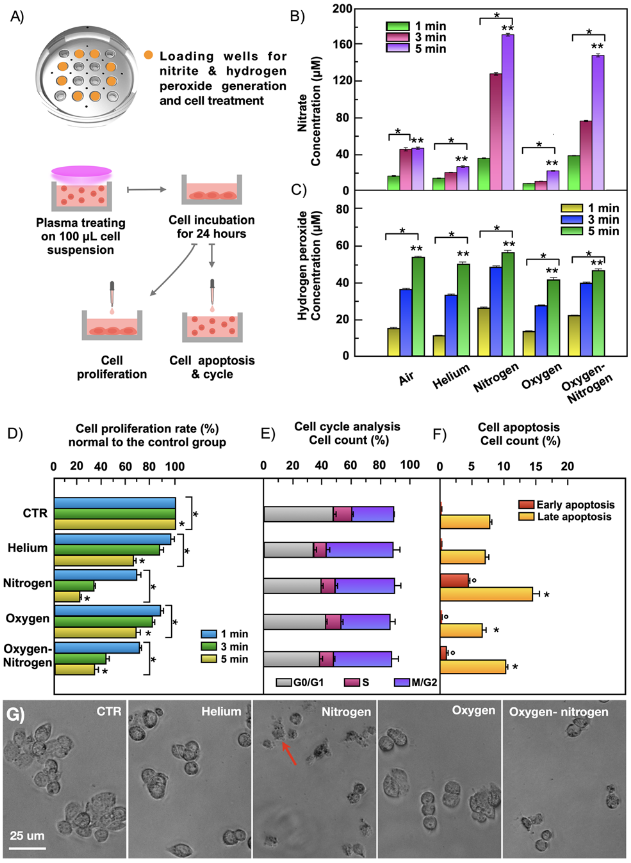

Fig. 4 Cell response discrimination *via* tuning the plasma feed gas mixture for functional species identification. (A) Schematic of sample loading positions and treatment procedures. (B) NO_2 generation in 100 μL PBS after plasma treatment. (C) H_2O_2 generation in 100 μL PBS after plasma treatment. (D) Cell proliferation rate (normal to the control group). (E) Cell cycle distribution. (F) Cell apoptosis triggering. (G) Cell morphology transformation after the treatment of different plasmas for 5 min (the scale bar is the same for the five pictures). Cell suspension (5×10^4 cells/100 mL DMEM) was transferred into pre-sterilized glass receptacles before plasma treatment. After the treatment by the different types of plasmas, cells were incubated for 24 hours for subsequent analysis. Samples in control groups were treated with the feed gas for the same duration without plasma excitation. Data are presented as mean ± SD. All experiments were conducted in triplicate and repeated three times. Statistical significance was calculated *via* the nonparametric Kruskal–Wallis test for multiple comparisons. $^*p < 0.05$, $^\circ p < 0.05$, $^{**}p < 0.01$.

the control group, the treatment of helium plasma decreases cell proliferation to 95.92%, 86.54%, and 65.16% for 1 min, 3 min, and 5 min, respectively (Fig. 4D). Oxygen plasma presents an approximate level of cell growth reduction as helium plasma (87.6% for 1 min, 80.80% for 3 min, and 67.37% for 5 min). However, the introduction of nitrogen gas makes the nitrogen and oxygen–nitrogen plasma block cell growth much more significantly. After the treatment of nitrogen plasma for 1 min, 3 min, and 5 min, the cell proliferation is reduced to 67.86%, 32.99%, and 21.34%, respectively. Similarly, the proliferation rate obtained after the treatment of oxygen–nitrogen plasma is 70% for 1 min, 42.53% for 3 min, and 33.32% for 5 min. Exposure to a high concentration of ROS, such as atomic oxygen, superoxide, singlet oxygen, and hydrogen peroxide, can damage cells.[50–53] In our experiment, helium and oxygen plasma indeed restrict cell growth to some extent, indicating the impact of the ROS. However, the severe effects of the nitrogen and oxygen–nitrogen plasma strongly indicate that the role of the RNS (NO, NO_2^-/NO_3^-, $ONOO^-$) cannot be neglected. Besides, we also analysed the cell cycle distribution after plasma treatment, since regular cell cycle progression drives cell renewing.[54,55] We find cell cycle arrests in M/G2 phase with cells located in the G0/G1 phase reduced after 5 min treatment compared with the control group (Fig. 4E and ESI† Appendix, Fig. S8). The broken cell phase distribution balance predicts a decrease of cell growth after plasma treatment.

Cell apoptosis stimulation has been proposed as one of the main mechanisms of the anticancer effect of plasmas. Unlike other types of cell death,[56] cell apoptosis does not cause inflammation, protecting the surrounding healthy cells or tissues.[57] Due to this feature, cell apoptosis stimulation is preferred in the oncotherapy.[58] In our work, after treatment for 5 min, nitrogen plasma stimulates the most apoptosis among cells (40 times and 20 times higher percentage of cells in early and late apoptosis respectively), followed by the oxygen–nitrogen plasma (10 times and 1.3 times higher percentage of cells in early and later apoptosis respectively) compared with the control group (Fig. 4F and ESI† Appendix, Fig. S9). Cell morphology transformations including cell detachment, cytosol shrinkage, and apoptotic bodies further prove the demonstrated cell apoptosis (Fig. 4G and ESI† Appendix, Fig. S10). No apparent apoptosis has been triggered after the treatment of helium and oxygen plasma. Although ROS has been demonstrated to cause cell death, we argue that the directly produced ROS in plasma here is insufficient to stimulate cell apoptosis.[59,60] The second produced ROS should most probably be the essential death driver. Some research results indicate that the singlet oxygen generated by the series of chemical reactions between hydrogen peroxide and nitrite should account for cell death.[61,62] Given the higher level of hydrogen peroxide and nitrite production, the severe influences on cell growth inhibition and apoptosis stimulation of the nitrogen and oxygen–nitrogen plasma could also be in support of this hypothesis. Therefore, to successfully apply plasma oncotherapy, nitrogen gas should be introduced as part of plasma source gases. The diverse sensitivity of the HepG2 cells towards the plasmas fed with different gas mixtures illustrates the effectiveness of tuning plasma constitutions to study their specific roles. Further development of the proposed chip could possibly enable further investigation of new plasma-induced anticancer mechanisms.

Demonstration of multiplex treatment strategies

Since plasma therapeutical effects largely depend on cell sensitivity,[27] it is better to single out the more vulnerable

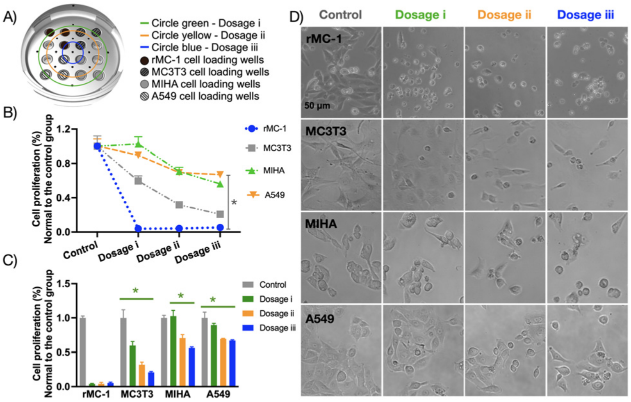

Fig. 5 Illustration of the multiplex treatment strategy. (A) Schematic of cell loading pattern on the multi-sample holding sheet. (B) The strategy of multi-sample treatment: compare the susceptibility of various cell lines with one-time treatment. (C) The strategy of multi-dosage treatment: optimize the treatment dosage from the imposed three level dosages. (D) Cell morphology transformation after nitrogen plasma treatment for 1 min (the scale bar is the same for all the pictures). 2 × 10^5 cells suspended in 100 μL PBS were radiated by nitrogen plasma for 1 min. 1 × 10^4 cells were seeded in each well in a 96-well plate. Cell proliferation rates were measured after 24 hours of incubation. All experiments were conducted in triplicate and repeated three times. Data are presented as mean ± SD. Statistical significance was calculated *via* the nonparametric Kruskal Wallis test for multiple comparisons. *$p < 0.05$.

cells to apply plasma oncotherapy. Also, an appropriate dosage should be applied for optimal efficacy.[63] To apply plasma oncotherapy, the appropriate treatment dosage must be optimized. Assisted by our device, at one-time radiation, we can compare the susceptibility of multiple cell lines towards plasma treatment. Moreover, we can analyse cell responses at three treatment dosages to explore the optimized treatment dosage for plasma oncotherapy. As shown in Fig. 5A, four types of cell lines including retinal Müller cell rMC-1, pre-osteoblast cell MC3T3, immortalized liver cell MIHA, and lung cancer cell A549 were loaded (Fig. 5A) and treated by the nitrogen plasma to demonstrate the multiplex treatment potentialities. The multi-sample treatment capability can be demonstrated by the distinct susceptibility of the four tested cell lines. After 1 min treatment, we can clearly see that rMC-1 cells are the most vulnerable to plasma treatment, followed by the MC3T3 cell line under all the three-level dosages (Fig. 5B). Cell skeleton disruption and cytosol shrinkage shown in Fig. 5D further prove the huge influences of the nitrogen plasma treatment. By contrast, the MIHA and A549 cell lines are relatively resistant to plasma treatment. The multi-dosage treatment strategy can be demonstrated by the graded proliferation rate of the MIHA cell line. After 1 min treatment, we find cell proliferation rate can be assorted to 3 grades by the current-settled three dosage levels (Fig. 5C). The defined dosage iii suppresses cell growth the most (56.2%), followed by dosage ii (70.6%) and dosage i (102.6%). Referred to desired cell proliferation rate for target research, the appropriate treatment dosage can be chosen. The same rules could be followed to analyse the MC3T3 and A549 cell lines. In the case of rMC-1 cell line, we may decrease the input power to reduce plasma strength overall, allowing cell proliferation to be graded. The established strategy of multi-sample treatment can efficiently isolate the more vulnerable cell lines for plasma oncotherapy. The multi-dosage treatment strategy can optimize the appropriate dosage for exposed cancer cells to direct the clinical application of plasma-based oncotherapy. In addition to the study on standard two-dimensional cell culture, our device can also be extended to three-dimensional models and diseased tissue (*ex vivo*) investigation. Treatment results on cellular spheroids or even organoids can provide more representative guidelines for the clinical application, due to the more accurate tumor environment simulation.[64] Tissue exposure can help evaluate the damage of plasma treatment at an *ex vivo* level and explore the penetration depth of the different plasma compositions.[64–66]

Conclusions

Since the existing plasma exposure devices fail to controllably produce targeted species, experimental verification of the plasma-induced anticancer mechanisms remains challenging. The restrained single sample processing capacity further hampers the appropriate treatment dosage optimization and the selection of vulnerable cell lines for plasma oncotherapy application. To elucidate the underlying anticancer mechanisms and realize the clinical application of plasma oncotherapy, specifically designed devices are warranted. This study proposes a composition-tunable cold atmospheric plasma chip for multiplex treatment on cells. The environment control module protects the plasma plump from air species contamination and reduces the surrounding environmental influences on plasma igniting. Without air species invasion, the plasma components can be precisely controlled and modulated. Targeted species exposure on cells can be achieved and the specific role of different targeted species can be identified and explained. The multi-inlet gas-feed module facilitates the uniform distribution of the feed gas, stabilizing and evenly distributing the produced plasma along concentric circles. Hence, uniform treatment is attained to force cells to respond consistently for reliable results obtaining. The multi-inlet gas feed module and multi-sample holding module coordinately achieve the multiplex treatment: multi-sample and multi-dosage treatment at one-time radiation. Such capacity enables our chip to single out the more vulnerable cancer type and the applicable treatment dosages efficiently to apply plasma oncotherapy. By treating the liver cancer cell line, we find the introduction of nitrogen in feed gas can effectively inhibit cell proliferation and trigger apoptosis. Such a result, on the one hand, points out the nonnegligible role of the nitrogen-based species in plasma oncotherapy, on the other hand, suggests that tuning plasma components is imperative to understanding the roles of the species. By loading four types of cell lines on wells standing on the three concentric circles, we prove that cell susceptibility of the under-analyzed cell lines can be compared with one-time treatment. Also, three-level treatment dosages can be imposed to analyze cell responses for appropriate dosage selection to direct the clinical application of plasma oncotherapy. As we discussed above, the current sample layout pattern can be further enlarged or improved to support the target research. The multi-dosage and multi-sample design strategy will suggest a new direction for the development of plasma exposure devices, inspiring the clinical application of plasma-based oncotherapy.

Materials and methods

Configurations of the cold plasma chip

The plasma igniting chip mainly consisted of power electrode and ground electrode (PE and GE, Fig. 1B:5 and 8), acrylic insulator sheet (white sheet between the discharge electrodes, Fig. 1A), dielectric barrier sheet (Fig. 1B:6), 10 mm thick quartz sheet (Fig. 1B:4) and cover acrylic sheet (white sheet above PE), as shown schematically in Fig. 1A and B. Electrodes were made from aluminum, while the dielectric barrier sheet was made from quartz. In addition to the dielectric barrier sheet, all the above-mentioned parts were fastened tightly by screws to form the outer shell of the device with seal rings applied to ensure good tightness. The as-obtained sealed interior cavity of the chip and a vacuum pump (2546C-02W, Welch, Germany) constituted the environment module. Before plasma igniting, the residual air in the chip was removed and the space was refilled with high purity feed gases. The whole process was monitored by a barometer (ZSE 30AF-01-N, SMC, Japan). Three types of high purity (99.999%) gases of helium, nitrogen, and oxygen were injected into the chip with the flow speed monitored and modulated by flowmeters (Fujikin, FCST, Japan). 8 central-symmetrically arranged gas-tube adaptors mounted on GE worked as gas inlets. Feed gas flew into the chip *via* the 8 inlets and arrived at the space above PE, which space was defined as the gas input cavity (Fig. 1B:1). The 8 inlets and the gas input cavity constituted the multi-inlet gas-feed module (Fig. 1D). 16 airholes were manufactured on the PE. *Via* the airholes, the feed gas could diffuse from the input cavity to the slim space between the discharge electrodes, which space was defined as the discharge cavity (Fig. 1B:2). Under the discharge region was the multi-sample holding module (Fig. 1C), which contained 16 sample-holding wells and glass receptacles (Fig. 1B:9) with a volume of 100 mL. The sample holding wells were manufactured and central-symmetrically arranged on the GE. While the glass receptacles were in the wells to accommodate the biological samples (Fig. 1B:10). In this work, a radio frequency power (AG 0613 RF POWER SOURCE, T&C Power Conversion, USA) was connected to the electrodes. When the appropriate potential was applied, the plasma was excited (Fig. 1B:7) and the samples in the receptacle were radiated. An oscilloscope (MDO34, Tektronix, USA) was used to record current and voltage variations. Surplus feed gas flew out of the device *via* the gas channels (Fig. 1B:3), which connected with another 8 gas-tube adaptors working as gas outlets. At the bottom of the GE, another aluminum sheet with a water reservoir was included. Powered by a peristaltic pump, the ice-cold water kept cycling carrying away the accumulated heat in the GE. Temperature changes of the electrodes were recorded by an infrared thermometer camera (T660, FLIR, USA).

Optical emission spectra

The excited species were identified by a spectrometer (USB4000, Ocean Optics, USA). The optic lens was fixed by a mechanical arm at 1 mm above the observation window (the 10 mm thick quartz sheet), concentrically with one of the airholes. The integration time of the spectrometer was set to 100 ms. The average of intensities was calculated from 5 repeated emission spectra.

COMSOL simulation

A three-dimensional gas flow model built in Creo 3.0 software (ESI† Appendix, Fig. S1a) was transferred to COMSOL 5.0 for gas flow state simulation. In view of the symmetric feature of the model, a quarter of the gas model was simulated (ESI† Appendix, Fig. S1b). In simulations, a 500 sccm flow velocity boundary condition was applied at the inlets, and a pressure of 0 MPa relative to the atmospheric pressure at the outlets was imposed with backflow suppressing definition. Standard helium gas defined in the software was used in this calculation. Navier–Stokes equation was selected to calculate the model.

Cell culture and plasma treatment

Human liver cancer cell line (HepG2), immortalized liver cell line (MIHA), retinal Müller cells (rMC-1), and human lung cancer cell line (A549) were cultured in a 10 mm culture dish with high-glucose DMEM (10-013-CVRC, Corning, USA), 10% fetal calf serum (35-081-CV, Corning, USA), and 1% penicillin–streptomycin (30-002-CL, Corning, USA). Mouse pre-osteoblast (MC3T3) cell line was cultured in MEM (2416807, Gibco, USA) with 10% fetal calf serum and 1% penicillin–streptomycin. Cells were incubated in a humidified incubator at 37 °C with 5% CO_2. When 70% confluence was reached, cells were washed with phosphate buffer saline solution (PBS, 21-040-CV, Corning, USA) and harvested with Trypsin (25-053-CL, Corning, USA) for plasma treatment.

Quantification of H_2O_2 and NO_2^- generation

The H_2O_2 generation in plasma-activated PBS was quantified using the fluorometric H_2O_2 assay kit (MAK165, Sigma-Aldrich, USA). Plasma-activated 50 mL PBS solution was mixed with 50 mL of the working solution prepared according to the manufacturer's instructions, and the mixture was incubated in darkness at room temperature for

30 min. A microplate reader (EnSpire, PerkinElmer, USA) detected the fluorescence intensity at the excitation/emission wavelength of 540 nm/590 nm. The NO_2^- concentration in plasma-activated PBS was measured using the Griess Reagent System (G2930, Promega, USA). According to the manufacturer's protocol, 50 mL plasma-activated PBS solution was firstly mixed with 50 mL sulfanilamide solution and incubated in darkness at room temperature for 7 min. Then 50 mL NED solution was added to the mixture and incubated in darkness at room temperature for another 7 min. A microplate reader (SpectraMax 190, Molecular Device, USA) was utilized to detect the light absorbance at the wavelength of 530 nm.

Cell proliferation

The cell proliferation rate was quantified using the CCK-8 cell counting kit (K1018, ApexBio, China). After plasma treatment, 1×10^4 cells were seeded in each well of a 96-well plate for further incubation. After 24 hours, the original culture medium was replaced by 100 mL fresh medium (10% CCK-8) in each well, and cells were further incubated in darkness at 37 °C for 2 hours. The microplate reader (SpectraMax 190, Molecular Device) was utilized to measure the light absorbance at the wavelength of 450 nm.

Cell apoptosis assay

Cell apoptosis was characterized with the Annexin V-FITC/PI Apoptosis Detection Kit (ma0220, Meilumbio, China). After plasma treatment, 2×10^5 cells were seeded in a 3 mm culture dish. 24 hours later, cells were harvested. 1×10^5 cells were suspended in a 500 mL working buffer solution with 5 mL Annexin V and 10 mL propidium iodide (PI) solution added to stain the cells. The fluorescence was detected by a Flow cytometer (FACSCanto, BD, USA), and the data were analyzed by FlowJo software (BD, USA).

Cell cycle assay

Plasma-treated cell solution containing 2×10^5 cells was collected and incubated in a 3 mm culture dish. After 24 hours of incubation, cells were harvested, washed, and fixed with 1 mL 75% ice-cold ethanol at 4 °C overnight. After fixed, 1×10^5 cells were washed twice and resuspended in a 500 mL staining solution which contained 10 mL RNase (R1030-1, Solarbio, China), 10 mL PI (CA1020-20, Solarbio, China), and 480 mL PBS. The same cytometer (FACSCanto, BD, USA) was used to measure the fluorescence intensity. According to DNA content, cell cycle distribution was analyzed with the FlowJo software (BD, USA).

Statistical analysis

All results are presented as means ± SD or as means ± SEM. Nonparametric Kruskal Wallis tests were applied for multiple comparisons. All statistical analyses were carried out with Origin software. The threshold for statistical significance was $P < 0.05$.

Author contributions

Conceptualization: Fang Wang, Hui Deng; data curation, formal analysis: Wang Fang; funding acquisition: Hui Deng, Ho Cheung Shum; investigation, methodology, project administration, resources, software, validation, visualization: Fang Wang; supervision: Hui Deng, Ho Cheung Shum; writing–original draft: Fang Wang; writing–review & editing: Fang Wang, Chang Li, Ruotong Zhang, Yuan Liu, Lang Nan, Haisong Lin, Muhammad Ajmal Khan, Yang Xiao, Ho Cheung Shum. All authors have read and agreed to the published version of the manuscript.

Conflicts of interest

H. C. Shum is a scientific advisor of EN Technology Limited in which he owns some equity, and a managing director of the research center, namely Advanced Biomedical Instrumentation Center Limited. The work in the paper is however not directly related to the works of these two entities, as far as we know. The authors have applied for a patent for this plasma chip.

Acknowledgements

The authors acknowledge the assistance of SUSTech Core Research Facilities and express their appreciation to Prof. Qiongyu Guo (Department of Biomechanical Engineering, SUSTech) for providing the human liver cancer cell line (HepG2), Dr. Alan Wong (School of Biomedical Sciences, HKU) for providing Lung cancer cell line A549 and immortalized human liver cell line MIHA, Dr. Yau Kei Chan (Department of Ophthalmology, HKU) for providing the retinal Müller cell line rMC-1, and Prof. James Kit Hon Tsoi (Faculty of Dentistry, HKU) for providing the pre-osteoblast cell line (MC3T3) to support our research. This work is supported by the following funding: National Natural Science Foundation of China (NSFC) (52035009, 52005243); NSFC Excellent Yong Scientists Fund (Hong Kong and Macau) (21922816); Science and Technology Innovation Committee of Shenzhen Municipality (JCYJ20200109141003910, JCYJ20210324120402007, KQTD20170810110250357); Platform Technology Funding from the University of Hong Kong. H. C. Shum was supported in part by the Croucher Foundation through the Croucher Senior Research Fellowship.

References

1 G. Sgouros, L. Bodei, M. R. McDevitt and J. R. Nedrow, *Nat. Rev. Drug Discovery*, 2020, **19**, 589–608.
2 J. A. Myers and J. S. Miller, *Nat. Rev. Clin. Oncol.*, 2021, **18**, 85–100.
3 J. L. McQuade, C. R. Daniel, B. A. Helmink and J. A. Wargo, *Lancet Oncol.*, 2019, **20**, e77–e91.

4 W. C. Hahn, J. S. Bader, T. P. Braun, A. Califano, P. A. Clemons, B. J. Druker, A. J. Ewald, H. Fu, S. Jagu, C. J. Kemp, W. Kim, C. J. Kuo, M. McManus, G. B. Mills, X. Mo, N. Sahni, S. L. Schreiber, J. A. Talamas, P. Tamayo, J. W. Tyner, B. K. Wagner, W. A. Weiss, D. S. Gerhard, D. Cancer Target and N. Development, *Cell*, 2021, **184**, 1142–1155.

5 X. Guo, N. Yang, W. Ji, H. Zhang, X. Dong, Z. Zhou, L. Li, H. M. Shen, S. Q. Yao and W. Huang, *Adv. Mater.*, 2021, **33**, e2007778.

6 M. Keidar, *Plasma Sources Sci. Technol.*, 2015, **24**, 033001–033020.

7 M. Mateu-Sanz, J. Tornin, M. P. Ginebra and C. Canal, *J. Clin. Med.*, 2021, **10**, 893.

8 X. Dai, K. Bazaka, E. W. Thompson and K. K. Ostrikov, *Cancers*, 2020, **12**, 3360.

9 E. A. Ratovitski, X. Cheng, D. Yan, J. H. Sherman, J. Canady, B. Trink and M. Keidar, *Plasma Processes Polym.*, 2014, **11**, 1128–1137.

10 N. Barekzi and M. Laroussi, *Plasma Processes Polym.*, 2013, **10**, 1039–1050.

11 J. H. S. Dayun Yan and M. Keidar, *Oncotarget*, 2017, **8**, 15977–15995.

12 M. Ishaq, M. M. Evans and K. K. Ostrikov, *Int. J. Cancer*, 2014, **134**, 1517–1528.

13 D. Yan, A. Horkowitz, Q. Wang and M. Keidar, *Plasma Processes Polym.*, 2021, **18**, e2100020.

14 C. Tendero, C. Tixier, P. Tristant, J. Desmaison and P. Leprince, *Spectrochim. Acta, Part B*, 2006, **61**, 2–30.

15 A. von Keudell and V. Schulz-von der Gathen, *Plasma Sources Sci. Technol.*, 2017, **26**, 113001.

16 P. J. Bruggeman, F. Iza and R. Brandenburg, *Plasma Sources Sci. Technol.*, 2017, **26**, 123002.

17 X. Lu, G. V. Naidis, M. Laroussi, S. Reuter, D. B. Graves and K. Ostrikov, *Phys. Rep.*, 2016, **630**, 1–84.

18 D. B. Graves, *J. Phys. D: Appl. Phys.*, 2012, **45**, 263001.

19 F. A. Villamena, *Molecular Basis of Oxidative Stress*, Wiley, U.S.A., 2013.

20 A. Privat-Maldonado, C. Bengtson, J. Razzokov, E. Smits and A. Bogaerts, *Cancers*, 2019, **11**, 1920.

21 S. Mitra, L. N. Nguyen, M. Akter, G. Park, E. H. Choi and N. K. Kaushik, *Cancers*, 2019, **11**, 1030.

22 N. K. Kaushik, B. Ghimire, Y. Li, M. Adhikari, M. Veerana, N. Kaushik, N. Jha, B. Adhikari, S. J. Lee, K. Masur, T. von Woedtke, K. D. Weltmann and E. H. Choi, *Biol. Chem.*, 2018, **400**, 39–62.

23 G. Bauer, *Redox Biol.*, 2019, **26**, 101291.

24 N. Kurake, H. Tanaka, K. Ishikawa, T. Kondo, M. Sekine, K. Nakamura, H. Kajiyama, F. Kikkawa, M. Mizuno and M. Hori, *Arch. Biochem. Biophys.*, 2016, **605**, 102–108.

25 T. I. Pavlik, N. G.-o. Gusein-zade, L. V. Kolik and N. L. V. Shimanovskii, *Appl. Sci.*, 2022, **12**, 3704.

26 G. Bauer, *Anticancer Res.*, 2016, **36**, 5649–5663.

27 D. Yan, A. Talbot, N. Nourmohammadi, J. H. Sherman, X. Cheng and M. Keidar, *Biointerphases*, 2015, **10**, 040801.

28 Q. Wang, A. Malyavko, D. Yan, O. K. Lamanna, M. H. Hsieh, J. H. Sherman and M. Keidar, *J. Phys. D: Appl. Phys.*, 2020, **54**, 095207.

29 D. Yan, Q. Wang, M. Adhikari, A. Malyavko, L. Lin, D. B. Zolotukhin, X. Yao, M. Kirschner, J. H. Sherman and M. Keidar, *ACS Appl. Mater. Interfaces*, 2020, **12**, 34548–34563.

30 D. B. Graves, *Plasma Processes Polym.*, 2014, **11**, 1120–1127.

31 X. Dai, Z. Zhang, J. Zhang and K. Ostrikov, *Plasma Processes Polym.*, 2020, **17**, e1900178.

32 E. Gjika, S. Pal-Ghosh, A. Tang, M. Kirschner, G. Tadvalkar, J. Canady, M. A. Stepp and M. Keidar, *ACS Appl. Mater. Interfaces*, 2018, **10**, 9269–9279.

33 M. Keidar, D. Yan, I. I. Beilis, B. Trink and J. H. Sherman, *Trends Biotechnol.*, 2018, **36**, 586–593.

34 Y. G. Abraham Lin, J. De Backer, J. Van Loenhout, W. Van Boxem, F. Lemière, P. Cos, S. Dewilde, E. Smits and A. Bogaerts, *Adv. Sci.*, 2019, **6**, 1802062.

35 S. Bekeschus, R. Clemen, F. Niessner, S. K. Sagwal, E. Freund and A. Schmidt, *Adv. Sci.*, 2020, **7**, 1903438.

36 G. Chen, Z. Chen, D. Wen, Z. Wang, H. Li, Y. Zeng, G. Dotti, R. E. Wirz and Z. Gu, *Proc. Natl. Acad. Sci. U. S. A.*, 2020, **117**, 3687–3692.

37 Z. C. Guojun Chen, Z. Wang, R. Obenchain, D. Wen, H. Li, R. E. Wirz and Z. Gu, *Sci. Adv.*, 2021, **7**, eabg5686.

38 Z. Liu, D. Xu, D. Liu, Q. Cui, H. Cai, Q. Li, H. Chen and M. G. Kong, *J. Phys. D: Appl. Phys.*, 2017, **50**, 195204.

39 J. Kapaldo, X. Han and S. Ptasinska, *Plasma Processes Polym.*, 2019, **16**, 1800169.

40 M. Weiss, D. Gumbel, E. M. Hanschmann, R. Mandelkow, N. Gelbrich, U. Zimmermann, R. Walther, A. Ekkernkamp, A. Sckell, A. Kramer, M. Burchardt, C. H. Lillig and M. B. Stope, *PLoS One*, 2015, **10**, e0130350.

41 A. Azzariti, R. M. Iacobazzi, R. Di Fonte, L. Porcelli, R. Gristina, P. Favia, F. Fracassi, I. Trizio, N. Silvestris, G. Guida, S. Tommasi and E. Sardella, *Sci. Rep.*, 2019, **9**, 4099.

42 K. Nakamura, N. Yoshikawa, M. Yoshihara, Y. Ikeda, A. Higashida, A. Niwa, T. Jindo, H. Tanaka, K. Ishikawa, M. Mizuno, S. Toyokuni, M. Hori, F. Kikkawa and H. Kajiyama, *Plasma Processes Polym.*, 2020, **17**, 1900259.

43 X. Sole-Marti, A. Espona-Noguera, M. P. Ginebra and C. Canal, *Cancers*, 2021, **13**, 452.

44 G. Chehade, S. Lytle, H. Ishaq and I. Dincer, *Fuel*, 2020, **264**, 116831.

45 N. Knake, S. Reuter, K. Niemi, V. Schulz-von der Gathen and J. Winter, *J. Phys. D: Appl. Phys.*, 2008, **41**, 194006.

46 Z. Machala, B. Tarabova, K. Hensel, E. Spetlikova, L. Sikurova and P. Lukes, *Plasma Processes Polym.*, 2013, **10**, 649–659.

47 K. D. Weltmann, E. Kindel, T. von Woedtke, M. Hähnel, M. Stieber and R. Brandenburg, *Pure Appl. Chem.*, 2010, **82**, 1223–1237.

48 S. Moncada and J. D. Erusalimsky, *Nat. Rev. Mol. Cell Biol.*, 2002, **3**, 214–220.

49 G. Rhee Sue, *Science*, 2006, **312**, 1882–1883.

50 J. Wang and J. Yi, *Cancer Biol. Ther.*, 2008, **7**, 1875–1884.

51 D. Trachootham, J. Alexandre and P. Huang, *Nat. Rev. Drug Discovery*, 2009, **8**, 579–591.

52 C. Gorrini, I. S. Harris and T. W. Mak, *Nat. Rev. Drug Discovery*, 2013, **12**, 931–947.

53 L. Tong, C. C. Chuang, S. Wu and L. Zuo, *Cancer Lett.*, 2015, **367**, 18–25.

54 N. Hustedt and D. Durocher, *Nat. Cell Biol.*, 2016, **19**, 1–9.

55 T. Otto and P. Sicinski, *Nat. Rev. Cancer*, 2017, **17**, 93–115.

56 G. Majno and I. Joris, *Am. J. Clin. Pathol.*, 1995, **146**, 13.

57 S. Elmore, *Toxicol. Pathol.*, 2007, **35**, 495–516.

58 M. Garcia-Barros, F. Paris, C. Cordon-Cardo, D. Lyden, S. Rafii, A. Haimovitz-Friedman, Z. Fuks and R. Kolesnick, *Science*, 2003, **300**, 1155–1159.

59 M. Weiss, J. Barz, M. Ackermann, R. Utz, A. Ghoul, K. D. Weltmann, M. B. Stope, D. Wallwiener, K. Schenke-Layland, C. Oehr, S. Brucker and P. Loskill, *ACS Appl. Mater. Interfaces*, 2019, **11**, 19841–19853.

60 T. Wenzel, D. A. Carvajal Berrio, C. Reisenauer, S. Layland, A. Koch, D. Wallwiener, S. Y. Brucker, K. Schenke-Layland, E. M. Brauchle and M. Weiss, *Cancers*, 2020, **12**, 267.

61 P. M. Girard, A. Arbabian, M. Fleury, G. Bauville, V. Puech, M. Dutreix and J. S. Sousa, *Sci. Rep.*, 2016, **6**, 29098.

62 G. Bauer, *Redox Biol.*, 2019, **26**, 101301.

63 L. Feil, A. Koch, R. Utz, M. Ackermann, J. Barz, M. Stope, B. Kramer, D. Wallwiener, S. Y. Brucker and M. Weiss, *Cancers*, 2020, **12**, 1037.

64 F. Ruoff, M. Henes, M. Templin, M. Enderle, H. Bösmüller, D. Wallwiener, S. Y. Brucker, K. Schenke-Layland and M. Weiss, *Appl. Sci.*, 2021, **11**, 11238.

65 T. Wenzel, D. A. Carvajal Berrio, R. Daum, C. Reisenauer, K. D. Weltmann, D. Wallwiener, S. Y. Brucker, K. Schenke-Layland, E. M. Brauchle and M. Weiss, *ACS Appl. Mater. Interfaces*, 2019, **11**, 42885–42895.

66 J. Marzi, M. B. Stope, M. Henes, A. Koch, T. Wenzel, M. Holl, S. L. Layland, F. Neis, H. Bosmuller, F. Ruoff, M. Templin, B. Kramer, A. Staebler, J. Barz, D. A. Carvajal Berrio, M. Enderle, P. M. Loskill, S. Y. Brucker, K. Schenke-Layland and M. Weiss, *Cancers*, 2022, **14**, 1933.